Characteristics and controls of the runout behaviour of non-Boussinesq particle-laden gravity currents – A large-scale experimental investigation of dilute pyroclastic density currents

Journal of Volcanology and Geothermal Research 432 (2022) 107697

Contents lists available at ScienceDirect

Journal of Volcanology and Geothermal Research

journal homepage: www.journals.elsevier.com/journal-of-volcanology-and-geothermal-research

Characteristics and controls of the runout behaviour of non-Boussinesq particle-laden gravity currents – A large-scale experimental investigation of dilute pyroclastic density currents

E. Brosch [a,*], G. Lube [a], T. Esposti-Ongaro [b], M. Cerminara [b], E.C.P. Breard [c], E. Meiburg [d]

[a] Volcanic Risk Solutions, Massey University, Palmerston North, New Zealand
[b] Istituto Nazionale di Geofisica e Vulcanologia, Pisa, Italy
[c] University of Edinburgh, Edinburgh, United Kingdom
[d] University of California Santa Barbara, Santa Barbara, USA

ARTICLE INFO

Keywords:
Pyroclastic density current
Volcanic hazard
Gravity current
Non-Boussinesq
Froude number

ABSTRACT

One of the most dangerous aspects of explosive volcanism is the occurrence of dilute pyroclastic density currents that move at high velocities of tens to about a hundred of metres per second outwards from volcanic vents. Predicting the runout behaviour of these turbulent flows of hot particles and air is complicated by strong changes in the flow density resulting from entrainment of ambient air, sedimentation of particles, as well as heating and expansion of the gas phase. Current hazard models that are based on the behaviour of aqueous gravity currents cannot capture all aspects of the flow dynamics, and thus pyroclastic density current dynamics remain comparatively poorly understood. Here we interrogate the runout behaviour of dilute pyroclastic density currents in large-scale experiments using hot volcanic material and gas. We demonstrate that the flows transition through four dynamic regimes with distinct density and force characteristics. The first, inertial regime is characterized by strong deceleration under high density differences between the flow and ambient air where suspended particles carry a main proportion of the flows' momentum. When internal gravity waves start to propagate from the flow body into the advancing flow front, the currents transition into a second, inertia-buoyancy regime while flow density continues to decline. In this regime, subsequent arrivals of fast-moving internal gravity waves into the front replenish momentum and lead to sudden short-lived front accelerations. In the third regime, when the density ratio between flow and ambient air decreases closer to a value of unity, buoyancy forces become negligible, but pressure drag forces are large and constitute the main flow retarding force. In this inertia-pressure drag regime, internal gravity waves cease to reach the front. Finally, and with the density ratio decreasing below 1, the current transitions into a buoyantly rising thermal in regime 4.

Unlike for aqueous gravity currents, the Froude number is not constant and viscous forces are negligible in these gas-particle gravity currents. We show that, in this situation, existing Boussinesq and non-Boussinesq gravity current models strongly underpredict the front velocity for most of the flow runout for at least half of the flow propagation. These results are not only important for hazard mitigation of pyroclastic density currents but are also relevant for other turbulent gas-particle gravity currents, such as powder snow avalanches and dust storms.

1. Introduction

Dilute pyroclastic density currents (also dilute PDCs or pyroclastic surges and blasts) are frequent and lethal volcanic phenomena at the Earth's surface (Wohletz, 1998; Sulpizio et al., 2014; Lube et al., 2020), and they also occur at other terrestrial planets (Scott and Tanaka, 1982). Dilute PDCs constitute mobile and density-stratified multiphase flows of hot volcanic particles and air. They represent a type of particle-laden gravity current with significant density differences of the current to the ambient atmosphere (Burgisser and Bergantz, 2002). In this situation, suspended particles carry a significant proportion of the currents' momentum, and the gravity current behaviour and associated hazards

* Corresponding author.
E-mail address: e.brosch@massey.ac.nz (E. Brosch).

https://doi.org/10.1016/j.jvolgeores.2022.107697
Received 1 August 2022; Received in revised form 3 October 2022; Accepted 17 October 2022
Available online 21 October 2022

are strongly governed by the spatiotemporal evolution of suspended particles inside the flow. This situation is not unique to PDCs and similar, albeit isothermal processes are thought to occur in powder snow avalanches (Hopfinger, 1983; Ancey, 2004), in dust storms in deserts (Goudie and Middleton, 2001), in submarine turbidity currents (Meiburg and Kneller, 2010), and during the intrusion of heavy gases into air in environmental and industrial applications (Gröbelbauer et al., 1993).

Despite the omnipresence of gravity currents with high density differences (>10%) with their ambient medium in natural, environmental and industrial applications, the fundamental processes that govern their flow and hazard characteristics remain poorly understood (e.g. Birman et al., 2005; Lowe et al., 2005; Martin et al., 2006; Sovilla et al., 2008; Rotunno et al., 2011; Dai, 2014; Breard et al., 2016; Valentine and Sweeney, 2018; Pope et al., 2022). This differs from the understanding of compositional and particle-laden gravity currents with low density differences (<10%) between the current and ambient fluid, for which the Boussinesq approximation holds, which has strongly advanced during almost a century of investigation (von Karman, 1940; Benjamin, 1968; Huppert, 2006; Ungarish, 2009; Borden and Meiburg, 2013).

An important hazard characteristic of dilute PDCs (and PDCs in general), which is critical for estimating hazard impacts and risk, is the evolution of their frontal velocity during runout. Measurements of the front velocity of real-world dilute PDCs are extremely rare, and, as of today, satellite measurements of the position of the advancing front of the Mount St. Helens blast at a resolution of minutes remain the only detailed direct record (Moore and Rice, 1984). Aside from hazard considerations, and together with information of the evolving flow density, the kinematic characteristics of gravity currents can be used to interrogate the spatiotemporal evolution of force balances inside flows. For gravity currents with density differences between flow and ambient of less than *c.* 10%, and for which the Boussinesq approximation is assumed valid, experimentally-derived kinematic data allowed for the development of powerful analytical and numerical models (e.g. Huppert and Simpson, 1980; Harris et al., 2001). These Boussinesq models have been applied to turbidity currents, snow avalanches and PDCs alike to infer aspects of their flow and runout behaviours (e.g. Bursik and Woods, 1996; Dade and Huppert, 1996; Choux et al., 2004; Dufek, 2016; Shimizu et al., 2021). However, how well these models capture the behaviour of gas-particle gravity currents such as PDCs and snow avalanches, particularly during flow stages when density differences are high (non-Boussinesq), and what new phenomena occur in this situation remains largely unknown.

The ability to interrogate high-density gravity currents in large-scale experiments (Dellino et al., 2007; Andrews and Manga, 2012; Lube et al., 2015) and opportunities to measure inside real-world flows (Scharff et al. (2019), Brosch et al. (2021) for PDCs; Vriend et al. (2013), Sovilla et al. (2018) for snow avalanches; Hughes Clarke (2016), Azpiroz-Zabala et al. (2017) for turbidity currents) have provided new research avenues to bridge this gap in understanding.

This study interrogates the evolving runout behaviour of fully turbulent gas-particle gravity currents. Here, we simulate the natural behaviour of dilute PDCs by synthesizing PDC analogues of hot natural volcanic material and air in large-scale experiments. Our large-scale approach contrasts with the traditional experimental PDC analogue of aqueous (particle-laden) gravity currents (Huppert and Simpson, 1980; Bonnecaze et al., 1993). Results from these previous (lock exchange) experiments underpin the current concepts to model the structure, runout and hazard behaviour of dilute PDCs (Choux et al., 2004). Recently, however, a number of important shortcomings of the aqueous gravity current analogy to real-world PDCs have been pointed out (e.g. Burgisser et al., 2005; Andrews and Manga, 2012; Dellino et al., 2019; Brosch and Lube, 2020; Lube et al., 2020). A clarification of the implications of these limitations is also important to guide numerical modelling approaches aiming at estimating volcanic risk world-wide.

A subset of the experimental data analysed in this paper forms the first international benchmark case initiated through the Commission of Explosive Volcanism of the International Association of Volcanology and Chemistry of the Earth's Interior (IAVCEI). This benchmark serves the broader Volcanology community to test, validate and compare the current range of numerical PDC flow and hazard models.

2. Methods

The large-scale PDC experiments were conducted at the volcano simulator facility PELE in New Zealand. The set-up design, experimental procedure, sensor and measurement principles, as well as scaling similarity to real-world flows are presented in detail in Lube et al. (2015). Experimental PDCs are generated by dropping a heated mixture of natural pyroclastic material from an elevated hopper into an instrumented runout section. Following a brief period of vertical acceleration and mixing with colder ambient air during free-fall, the mixture forms a laterally moving particle-laden gravity current. Most of the data presented here focusses on an experiment with an initial particle mass of 124 kg at an initial temperature of 120 °C (while the ambient air temperature was 11 °C), and an initial drop height of 7 m (Supplementary Table 1 summarizes the experimental conditions). The volcanic material was a mixture of two facies of the AD232 Taupo ignimbrite deposit containing particle sizes in the range of 0.002 to 16 mm with the fraction of particles smaller than 64 μm accounting to *c.* 20 wt% (Supplementary Fig. 1). Details of the initial grain-size and particle density distribution are given in the Supplementary material. The hopper mass discharge, lasting *c.* 5 s, takes an approximately Gaussian form as a function of time, characterising a uni-modal discharge with an average of *c.* 20 kg s^{-1} and a peak value at roughly mid-discharge time of *c.* 44 kg s^{-1} (Supplementary Fig. 2).

The instrumented runout section has two differently inclined parts: a proximal 12.8 m-long, 6° inclined channel-confined section, and a 23 m-long, horizontal section, which is partially constrained (first 4 m). Where confined, the open channel is 0.5 m wide with variable tall side walls (0–6.4 m: 1.8 m high; 6.4–11.6 m: 1.2 m high; 11.6–16.8: 0.6 m high). A non-erodible bed roughness is created by gluing a close-packed bed of sub-rounded pebbles screened to 4–8 mm of long-axis diameter to the base.

The experiment is filmed with 22 cameras, three of which are high-speed cameras (spatial resolution: 2000 × 760 pixel; framerate 500 frames per second) for the calculation of vertical velocity profiles using particle-image velocimetry from high-speed videos through the tempered glass sides. The glass sides introduce boundary effects that do not occur in unconfined natural PDCs. In our experiments, we minimize these effects through the use of hydraulically smooth sidewalls. The thickness of the laminar layer is c. 500 μm, while the wall surface roughness has an average thickness of less than five microns. Furthermore, in our experiments, the Reynolds number, which is inversely related to the thickness of the viscous boundary layer, is high ($Re = 1.5 \times 10^6$). At regular runout distances, vertical profiles of particle solids-concentration, flow grain-size and temperature are obtained with details on the measurement principles given in the Supplementary Material.

The resulting gravity current is dynamically and kinematically well-scaled to natural PDCs. Table 1 shows a comparison of non-dimensional numbers for naturally occurring dilute PDCs and synthesised dilute PDCs. There is a good match as shown by the Reynolds numbers (a measure of turbulence intensity) reaching values of 1.5×10^6, Richardson numbers (characterising the stratification stability in turbulent flows) of 0.01–10, thermal Richardson numbers (measuring the ratio of forced and buoyant convection) of 0.02–4.5, Stokes numbers (characterising particle coupling to turbulent flow) of 10^{-3}–10^{0}, and Stability numbers (comparing velocities of particle settling relative to turbulent fluid motion) of 10^{-2}–10^{1}. We note that the range in Reynolds and Stokes numbers in nature can be significantly larger than in our experiments. Combined, the ranges in Reynolds, Stokes and Stability numbers allow for a complete range of gas-particle feedback

Table 1
Parameters for scaling experimentally generated dilute PDCs and their comparison to natural dilute PDCs.

Parameter	Definition	Dilute PDCs PELE	Dilute PDCs nature
Particle diameter	d	10^{-6}–10^{-2} m	10^{-6}–10^{-1} m
Solids density	ρ_S	350–2600 kg m^{-3}	300–2600 kg m^{-3}
Ambient density	ρ_A	0.8–1.2 kg m^{-3}	0.6–1.2 kg m^{-3}
Typical velocity	U	<0.5–9 m s^{-1}	10–100 m s^{-1}
Flow dynamic viscosity	μ_c	3×10^{-5}–3×10^{-3} kg m^{-1} s^{-1}	1×10^{-5}–4×10^{-3} kg m^{-1} s^{-1}
Kinetic energy density	$\frac{\rho_C U^2}{2}$	10^{-2}–10^{3} J m^{-3}	10^{3}–10^{4} J m^{-3}
Buoyant thermal energy density	$\rho_C \frac{C_{pc}}{C_{pA}} \alpha T g h$	10^{1}–10^{3} J m^{-3}	10^{3}–10^{4} J m^{-3}
Reynolds number	$\frac{\rho_C U h}{\mu_c}$	4.8×10^{4}–1.5×10^{6}	3.3×10^{6}–6.7×10^{9}
Richardson number	$\frac{\Delta \rho h g}{\rho_A U^2}$	0.01–10	0–10
Thermal Richardson number	$\frac{\Delta T \alpha h g}{U^2}$	0.02–4.5	0–5
Froude number	$\frac{U}{\sqrt{g' h \cos(\theta)}}$	0.75–2	~1
Stokes number	$\frac{U_T \Delta U_I}{\delta g}$	1×10^{-3}–9.9×10^{0}	1.1×10^{-3}–9.7×10^{7}
Stability number	$\frac{U_T}{\Delta U_I}$	1.3×10^{-2}–3.2×10^{1}	2.8×10^{-6}–9.7×10^{9}
Rouse number	$\frac{U_T}{k U_S}$	6.6×10^{-1}–1.9×10^{1}	10^{-3}–10^{2}

Where h is height; $\Delta\rho$ the difference between flow ρ_C and ambient density ρ_A; ΔT is the temperature difference between flow and ambient temperature; U_T is the terminal particle fall velocity; U_I is the eddy rotation velocity; U_S is the shear velocity; δ is the eddy diameter; α is the thermal air expansion coefficient; μ_c is the flow dynamic viscosity defined by Wohletz (1998) as $\mu_a * (1 + M)^2$ where μ_a is the dynamic viscosity of air and M the mass fraction ratio between ρ_S and ρ_A; C_{pC} and C_{pA} the bulk heat capacities of the flow and ambient, respectively; g is the acceleration due to gravity; g' is the reduced gravity; k is the von Karman constant; and θ is the slope. Scaling parameters for natural dilute PDCs are taken from Druitt (1998), Choux and Druitt (2002) and Burgisser et al. (2005).

mechanisms and turbulent particle transport.

3. Results

3.1. General flow characteristics

At the start of the experiment and hopper opening, the hot volcanic mixture accelerates vertically from a state of rest and loose packing (at *c.* 54 vol% solids concentration). At impact with the channel, the mixture attains a vertical velocity of *c.* 7 m s^{-1}, which is lower than the theoretical free fall velocity (c. 11.7 m s^{-1}) due to air drag during fall. The mixture then blasts laterally from the impact zone (also compare with Sweeney and Valentine (2017)), but the confining side-walls force it down the instrumented channel. At our first measurement location at a distance of two meters downstream of the channel start, the bulk flow concentrations decreased to *c.* 0.24 vol%.

A clearly defined gravity current structure forms approximately 0.35 s after impact (at a distance of *c.* 3.12 m), when expansion and entrainment have lowered the bulk flow concentration to *c.* 0.11 vol%, corresponding to a flow density of *c.* 3.4 kg m^{-3} and an initial density ratio between the flow and the ambient of approximately three. From here onwards, the propagating gravity current is highly turbulent with Reynolds number up to 10^6, and is composed of a leading, *c.* 1–2.5 m-thick *head* and a trailing, *c.* 1–1.6 m thick gravity current *body* (Fig. 1a and Supplementary Video). At the head, strong shear with the rough substrate and moderate shear with the ambient air generate an upstream directed rotating head vortex, which sheds off in its rear to feed a *c.* 1–2.5 m thick gravity current *wake*, which mantles and shields the body of the dilute PDC (Fig. 1a). The head is characterized by an overhanging nose, where the maximum frontal velocity is located, and a lobe-and-cleft structure due to entrainment and engulfment of ambient air immediately in front of the head. Interestingly, inside the body, a series of fast, downstream propagating pulses are clearly visible and audible (first documented in Brosch et al. (2021)). They appear as approximately bow-shaped regions of visibly higher particle concentration than flow regions immediately before and behind a pulse (Fig. 2). With an approximate period of slightly less than a second, a total of four to five such density discontinuities can be traced from *c.* 3–20 m runout length.

When the hopper discharge ceases at approximately five seconds, the gravity current has reached approximately half of its total runout length. At 23 s, the gravity current head stalls at a runout length of *c.* 32 m with gravity current lift-off continuing for at least another ten seconds. The gravity current deposit with a footprint of 300 m^2 can be traced and sampled up to 29 m downstream of the proximal impact region. The deposit thins from proximal, c. 0.2 m-thick, medium lapilli to fine ash sized massive to dune-bedded bedforms, to sub-millimetre thick laminated fine ash in distal reaches.

Fig. 3 illustrates the spatial evolution of the density ρ_C, velocity u_C and thickness h_C of the gravity current head. We define ρ_C as the depth- and time-integrated value of the flow density over the duration of the passage of the head at a measurement location; velocity u_C is the velocity of the head; and thickness h_C is the maximum head thickness at the centre of the head. ρ_C decreases strongly, and approximately following a power-law decay, with distance (Fig. 3a), which is associated with an approximately inverse relationship of the volume of aggrading deposit with time (Fig. 4). This demonstrates that, in addition to entrainment of ambient air and thermal expansion of the hot gas-particle mixture, the spatiotemporal sedimentation is critical to the evolving gravity current.

With regards to the evolving flow density, the gravity current runout may be subdivided into four stages (Fig. 3):

(i) up until 5.77–8.5 m, the declining ratio of the densities of the head and the ambient air ρ_C/ρ_A takes values greater than two. This non-Boussinesq stage is associated with a marked decrease in the flow front velocity u_F from *c.* 6.8–3.3 m s^{-1} and a strong increase in the thickness of the head from *c.* 1–2.2 m.

(ii) Further downstream and until *c.* 20 m, ρ_C decreases to c. 1.33 kg m^{-3} while the head (and entire body) throughout its entire height remains denser than the ambient air. In this stage, u_F decreases further from *c.* 3.3–2.5 m s^{-1}, while the head thickness systematically decreases from *c.* 2.2–1.1 m. Stage 2 is characterized by at least two distinct and sudden front accelerations (arrows in Fig. 3b). These brief accelerations are associated with the arrival of the fast-moving density discontinuities into the slower moving head.

(iii) At *c.* 22.6 m, the density ratio ρ_C/ρ_A has decreased to a value of *c.* 1.004. From here onwards the gravity current is composed of a lower part with local flow densities larger than that of the surrounding ambient air and an upper part with $\rho_C/\rho_A<1$, which strongly buoyantly expands (Fig. 1b).

(iv) At c. 29 m, the density ratio of the entire head is smaller than one and, together with the trailing body and wake, becomes thermally buoyant (Fig. 1c). In this phase of complete positive buoyancy, the flow does not advance further as a gravity current but expands at downstream velocities of a few decimetres per second during ascent of the buoyant phoenix cloud.

3.2. Dynamic phases

Most experiments on the propagation of density currents were conducted for aqueous density currents with density ratios close to unity. In this case, the Boussinesq approximation holds, and the kinematics of the head-dominated current can be expressed through the relative proportions of inertial, buoyancy and viscous forces. In this situation of aqueous gravity currents, increasing the density ratio through, for instance, adding large quantities of suspended sediment to the fluid, induces complex effects like formation of a slurry-like underflow

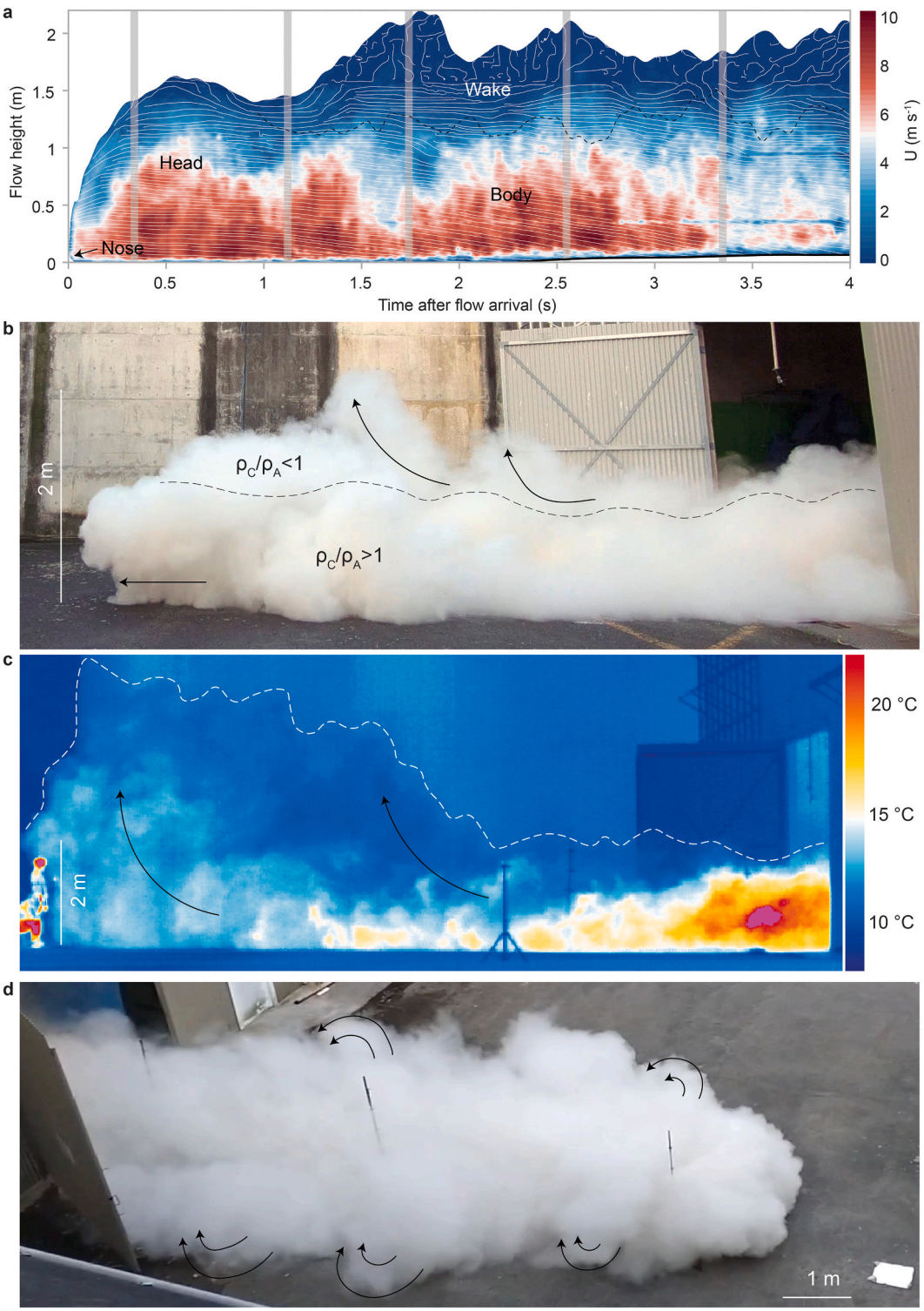

Fig. 1. Synthesizing dilute PDCs in large-scale experiments. **a.** Time-height contour plot of velocity magnitude and velocity streamlines at a static observer location at 3.12 m. Large-scale eddies are visible in the counterclockwise rotating head vortex and in the wake. The solid black line demarks the interface between the turbulent flow and aggrading deposit. The dashed black line marks the boundary between the body and wake regions. Semi-transparent grey bars mark the mapped duration of the passage of five density discontinuities associated with the fast-moving internal pulses.
b. Snapshot of the partially positively buoyant gravity current at unconfined propagation during density stage 3. The approximate boundary of the critical density ratio condition $\rho_C/\rho_A = 1$ is schematic only and based on measurements of dominant velocity vectors and time-integrated flow density measurements. **c.** Thermal infrared image of the fully positively buoyant gravity current at the beginning of the density stage 4. Note that the gravity current has transitioned into a series of buoyantly rising plumes. The dotted line demarks the upper boundary of this 'co-ignimbrite cloud'. **d.** Oblique birds' eye view of the hot gravity current during its unconfined propagation. The degree of axisymmetric spreading is limited to angles $<25°$. This is due to the self-confinement of the hot current due to a dominance of large vortices with an inward (towards flow centerline, that is counter clockwise on left and clockwise on right of current) rotation as previously documented in hot talc powder analogues for dilute PDCs (Andrews, 2014).

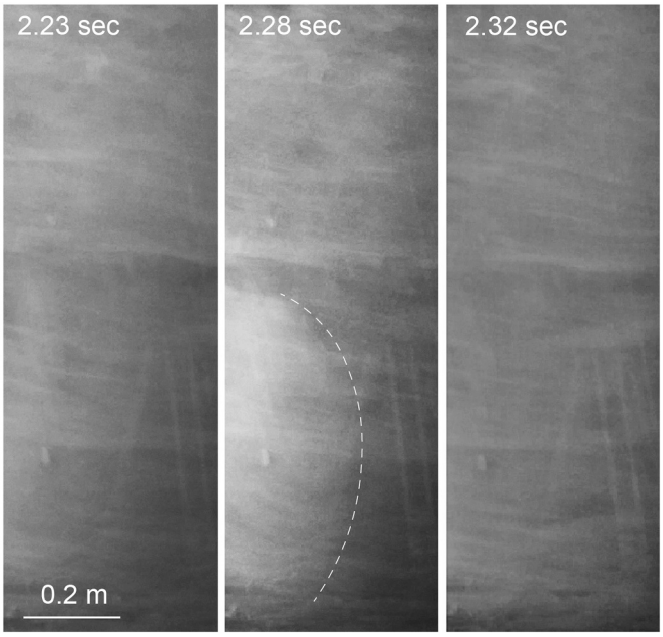

Fig. 2. Fast-moving density continuities during flow propagation (from left to right) at the static observer location 3.12 m. Three enhanced images of a high-speed video sequence depicting the lower 1.2 m of the gravity current at three different times immediately before, during and after passage of a density discontinuity. Dashed line highlights the upstream boundary of the bow-shaped density discontinuity, which moves at the speed of internal gravity waves through the advancing experimental PDC.

(Hallworth and Huppert, 1998) and abrupt transitions in propagation (Amy et al., 2005), which are not seen in the Boussinesq case. Comparably, little is known about the dynamic behaviour of heavy gas-particle gravity currents. Previous experiments on heavy gas intrusions were restricted to an early propagation stage only (Gröbelbauer et al., 1993). In the following, we describe the propagation of the experimental pyroclastic density currents through data of the kinematics of the gravity current head (Fig. 5).

Fig. 5a depicts the position of the flow front against time on linear scales. Overall, the kinematic pattern is characterized by a decelerating front with variable rates of deceleration. Fig. 5a also shows the positions of the five fast-moving density discontinuities (or pulses) against time (white circles in Fig. 5a). A subset of this data has already been presented in Brosch et al. (2021). Over the first approximately 15 m, the velocity of the density discontinuities is markedly constant at 6.72 m s^{-1}. Using simple dimensional analysis, Brosch et al. (2021) demonstrated that the density discontinuities move at the theoretical speed of internal gravity waves. Fig. 5a also shows that the first three of these internal pulses catch up and intrude into the leading front at approximately 1.3, 2.75 and 3.86 s after impact of the volcanic ash-air suspension with the channel (see arrows in Fig. 5a). The latter two pulses, however, slow down approximately 4–5 s after impact; they do not reach the gravity current front and cannot be traced beyond a runout distance of around 20 m.

Currently, the mechanism of formation of the fast-travelling density discontinuities (or internal gravity waves) cannot be captured by our experimental method and need further investigation. One possible explanation is the formation of weak shocks and supersonic instabilities after impact of the falling mixture with the channel, as seen in numerical simulations (Sweeney and Valentine, 2017; Valentine and Sweeney, 2018). While weak shocks and supersonic instabilities could occur on natural scales, our experimental PDCs are entirely subsonic. Another possibility includes the steepening and breaking of internal gravity waves, which may form immediately after impact when a strong vertical density stratification develops in the gravity current.

On logarithmic scales (inset in Fig. 5a), the distance against time data fall onto four subsequent linear segments highlighting four dynamic regimes of distinct rates of approximately constant deceleration. These dynamic regimes and regime boundaries are even more distinct on a logarithmic graph of the flow front velocity u_F against time (Fig. 3b). In analogy to aqueous gravity current experiments, we describe these four regimes together with data of the temporal variation of the densimetric Froude number in Boussinesq Fr' (von Karman, 1940; Benjamin, 1968) and non-Boussinesq Fr'' (Gröbelbauer et al., 1993; Nield and Woods, 2004) forms (Fig. 5b) defined as:

$$Fr' = \frac{u_C}{\sqrt{g h_C \frac{\rho_C - \rho_A}{\rho_A}}} \quad (1)$$

and

$$Fr'' = \frac{u_C}{\sqrt{g h_C \frac{\rho_C - \rho_A}{\rho_C}}}, \quad (2)$$

where g is acceleration due to gravity. Traditionally, for gravity currents with low density differences between flow and ambient medium, the Boussinesq form of the densimetric Froude number is applied (Eq. (1)). The densimetric Froude number Fr'' (non-Boussinesq form) accounts for a higher density difference between flow and ambient medium. Further, in Fig. 5c, we compare the four dynamic regimes together with estimates of the time-variant inertial force F_I, buoyancy force F_B, viscous forces F_V and pressure drag force F_D, defined as:

$$F_I = \rho_C u_C^2 h_C \, w \quad (3)$$

$$F_B = \rho_C g' h_C^2 \, w \quad (4)$$

$$F_V = \mu u_C L \frac{w}{h_C} \quad (5)$$

and

$$F_D = \frac{1}{2} \rho_A u_C^2 w h_C C_D \quad (6)$$

where w is the lateral width of the flow, g' is the reduced gravity defined in non-Boussinesq form as $g\left(\frac{\rho_C - \rho_A}{\rho_C}\right)$, μ is the dynamic viscosity, L the length of the gravity current and C_D the drag coefficient.

3.2.1. Dynamic regime 1 – inertial phase

After impact with the channel and up until c. 1.3 s (6.1 m), the gravity current head undergoes its strongest deceleration. On logarithmic scales, the distance against time data falls onto a line of slope 1 (inset Fig. 5a). The front velocity against time data, on logarithmic scales falls onto a line of slope − 1 with a best-fit through the data given by $u_F = 13.45t^{-1}$ (Fig. 3b). Regime I is characterized by vigorous entrainment into and thickening of the head, as well as the, above described, strong decrease in flow density due to rapid sedimentation. During regime I, both Froude numbers Fr' and Fr'' are supercritical and strongly decreasing (Fig. 5b). The inertial force markedly declines, but is significantly larger than buoyancy, viscous and drag forces (Fig. 5c).

3.2.2. Dynamic regime 2 – inertia-buoyancy phase

From *c.* 1.6–5.6 s (*c.* 6.5–22 m), overall, the distance vs. time data is well described by a linear segment with slope of 2/3 (inset in Fig. 5a), while the velocity vs. time data fall onto a line with slope of −1/3 with a best-fit through the data given by $u_F = 5.28t^{-1/3}$ (Fig. 3b). These distance-time and velocity-time power law relationships signify a balance of inertial and buoyancy forces (Huppert and Simpson, 1980) and have been observed in both Boussinesq compositional and non-Boussinesq particle-laden aqueous gravity currents (Amy et al., 2005).

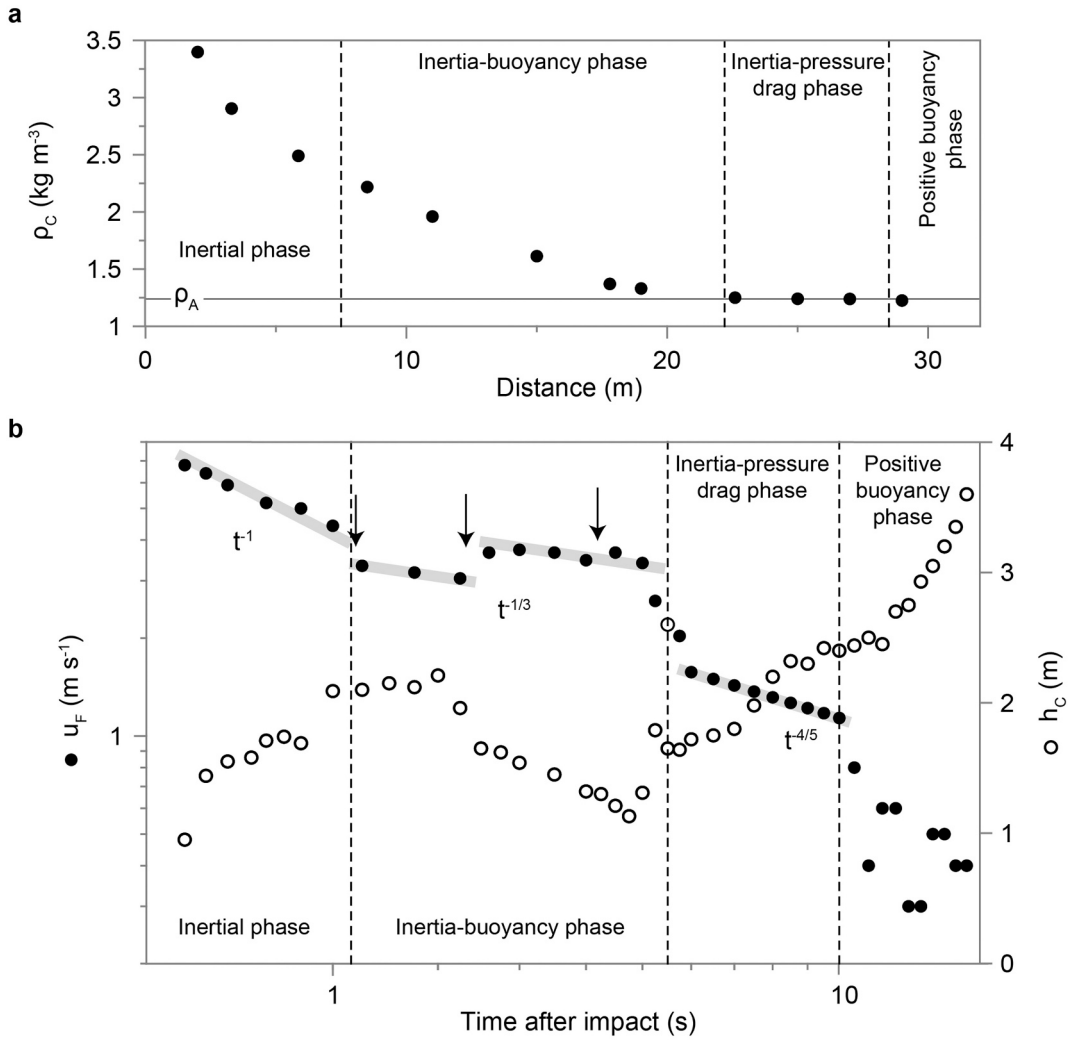

Fig. 3. Spatial variation of the density, velocity, and thickness of the head of the experimental PDC. **a.** depth- and time-integrated density of the head ρ_C against distance. The horizontal solid line marks the density of the ambient air ρ_A. The three vertical dashed lines delineate the four density stages described in the main text. They represent, in downstream order, $\rho_C/\rho_A = 2$, distinguishing non-Boussinesq from Boussinesq conditions; $\rho_C/\rho_A = 1.004$, downstream of which buoyancy forces are insignificant and the upper part of the gravity current starts to become positively buoyant; and $\rho_C/\rho_A = 1$, downstream of which the entire gravity current transforms into a buoyant co-ignimbrite cloud. **b.** The front velocity u_F and maximum height h_C of the head against time. Black arrows mark the points when internal density discontinuities migrate into the head and cause sudden and brief frontal accelerations. Note the general anticorrelation of head velocities and thicknesses during the four density stages. For further details, see main text.

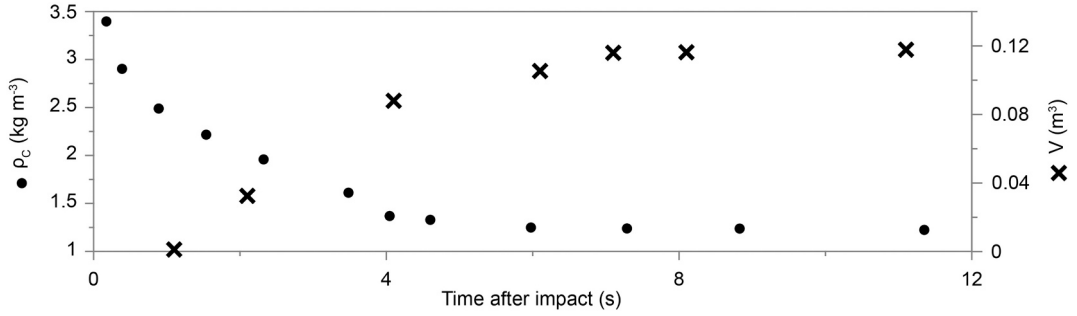

Fig. 4. Temporal evolution of the density of the advancing gravity current head ρ_C and the deposit volume V. Data of the density of the head (filled circle symbols, and same as in Fig. 3a) against time after impact of the volcanic ash-air mixture with the channel. Data of the cumulative volume of the aggrading PDC deposit (integrated over the spatially variable flow extent) against time (cross symbols). Time-variant deposit volume data are based on the measurements of the PDC deposit reported in detail in Brosch and Lube (2020). The two data series comprise a general anticorrelation, which highlights the control of time-variant particle sedimentation and deposition (rather than only entrainment of ambient air and thermal expansion) on the evolving flow density.

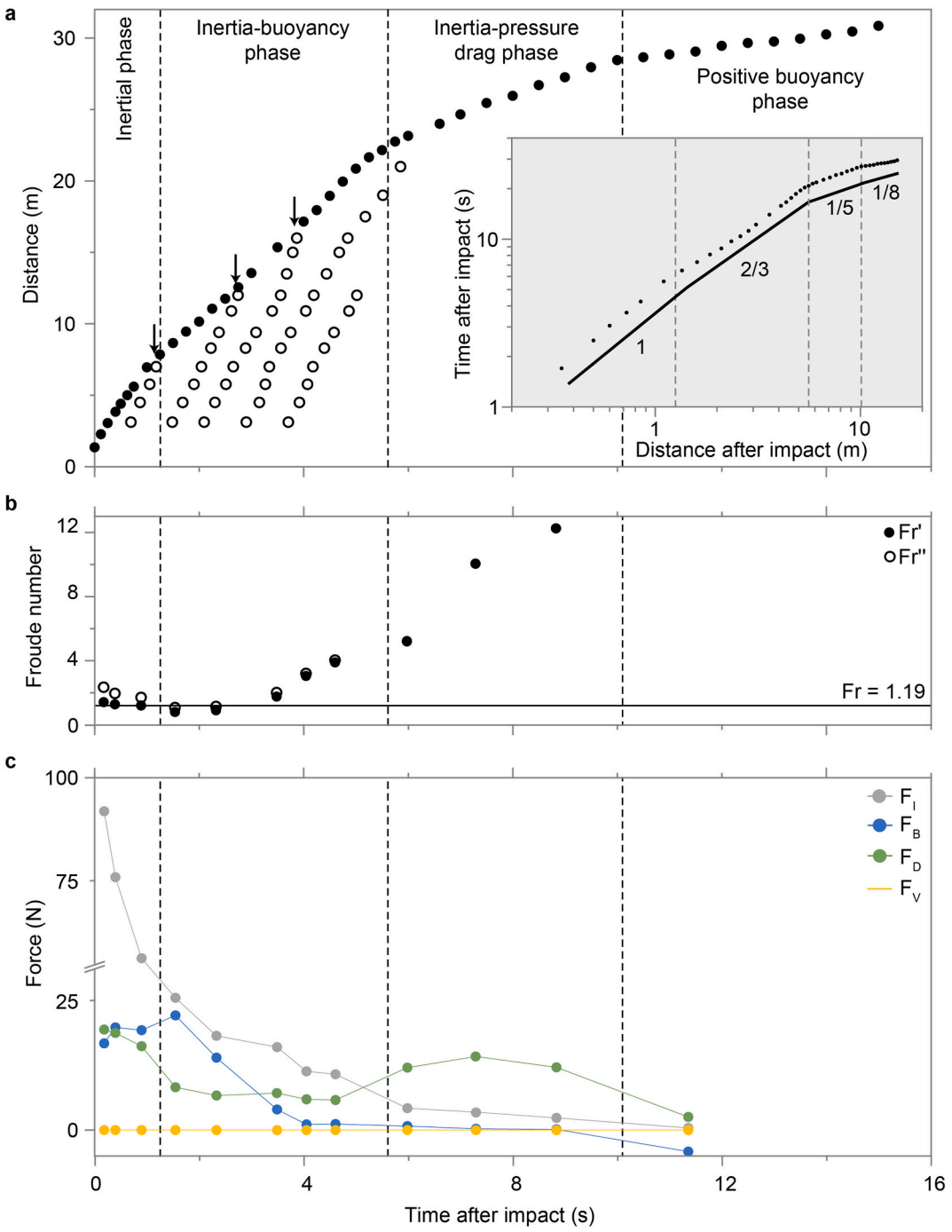

Fig. 5. Flow front kinematics in comparison to the spatial evolution of the characteristic non-dimensional velocity and characteristic flow forces. **a.** The position of the PDC front as a function of time on linear scales. Inset: log-log plot of the same data. The black straight lines show the alignment of data to four subsequent kinematic regimes with slopes of 1, 2/3, 1/5 and 1/8. The three vertical dashed lines in the linear version of the graph represent the times delineating these four dynamic regimes (inertial phase 1, inertia-buoyancy phase 2, inertia-pressure drag phase 3, and positive buoyancy phase 4) described in detail in the main text. Black arrows mark the arrival of internal density discontinuities into the flow front. **b.** Data of the densimetric Froude number in Boussinesq (Eq. (1)) and non-Boussinesq (Eq. (2)) forms against time, including the critical Froude number value of 1.19 (Huppert and Simpson, 1980). **c.** Data of estimates of the inertial force F_I (Eq. (3)), buoyancy force F_B (Eq. (4)) viscous drag force F_V (Eq. (5)), and pressure drag force F_D (Eq. (6)) against time. Note the variable dominance of the four different forces in each of the different dynamic regimes with details given in the main text.

In the first part of regime 2, inertial and buoyancy forces converge towards almost balanced conditions (Fig. 5c). This is associated with the Froude number approaching the critical value of 1.19 (Simpson and Britter, 1979; Huppert and Simpson, 1980) in the middle of this regime but Froude numbers increase again in the second half of regime 2 (Fig. 5b). This shows that, despite an overall convergence of the dominant inertial and buoyancy forces, the Froude number, unlike in aqueous gravity current experiments, is not a constant in regime 2.

The perturbation of a true inertia-buoyancy balance in regime 2 is associated with the arrival of internal density discontinuities into the head. The transition between regimes 1 and 2 coincides with the arrival of the first internal wave at *c.* 1.3 s (see arrows in Fig. 3b and Fig. 5a). Until then the gravity current is 'unaware' of its finite length. The arrivals of the second (*c.* 2.75 s) and third (*c.* 3.86 s) internal gravity waves

cause brief and sudden accelerations of the head. The brief accelerations are immediately followed by a return to constant deceleration characterized by slopes of the distance-time data of 2/3 on log-scales, albeit at a higher velocity caused by the acceleration.

3.2.3. Dynamic regime 3 – inertia-pressure drag phase

From *c.* 5.6–10.1 s (*c.* 22–28.5 m), the distance vs. time data, on log-log scales, is well approximated by a linear segment with slope of 1/5 (inset in Fig. 5a), while the velocity vs. time data fall onto a line with slope of −4/5 with a best-fit through the data given by $u_F = 8.29t^{-4/5}$ (Fig. 3b). These distance-time and velocity-time dependences are characteristic for the viscous-buoyancy phase in aqueous gravity currents in two-dimensional geometry and signify the flow regime when viscous forces become dominant. In dilute PDCs, and in our experimental PDCs, the viscous force is negligible. However, the transition between regimes 2 and 3 coincides with the time when the pressure drag force becomes large (Fig. 5c). This transition is also associated with the cessation of internal gravity waves propagating into and providing momentum into the head. In this regime, the gravity current has left the confining channel and is free to spread axisymmetrically. However, the degree of radial spreading of the hot currents is minimal and occurs on an average spreading angle of *c.* 23°. This 'self-confinement' of the strongly buoyantly rising current is associated with the inward rotation of the large peripheral vortices (Fig. 1d) and has been previously reported for the case of hot, experimental talc powder PDC analogues (Andrews, 2014).

During dynamic regime 3, sedimentation has advanced such that the density ratio ρ_C/ρ_A decreases below a value of 1.01 but remains above 1. Buoyancy forces are hence insignificantly small and the densimetric Froude numbers Fr' and Fr'' increase strongly to values greater than ten (Fig. 5b).

3.2.4. Dynamic regime 4 – positive buoyancy phase

From around 29 m onwards and, coinciding with the fourth density phase when the density ratio ρ_C/ρ_A, decreases below a value of 1 (see above), there is no more excess density driving the hot gravity current and it ascends as a thermal plume in analogy to the development of phoenix clouds in real-world PDCs. The outwards motion is solely due to the entrainment of ambient air into the thermal, and its consequent

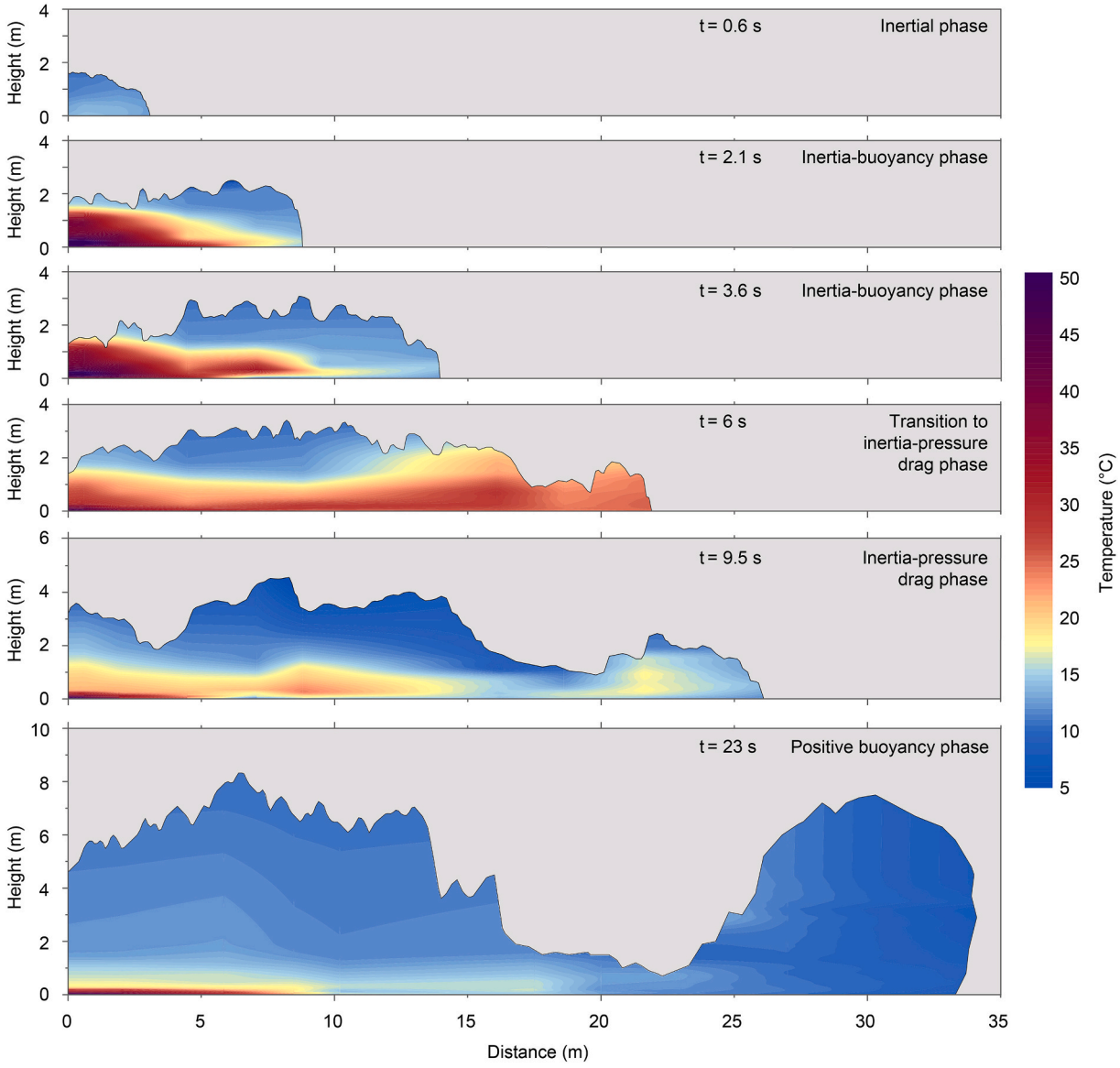

Fig. 6. Thermal characteristics of the advancing experimental PDC. Cross-sectional contour plots of the height- and downslope-variant flow temperature at six different times. The correspondence of these times to the four dynamic regimes is annotated and characteristics of the evolving thermal structure are given in the main text.

lateral expansion. For completeness, we add that the rate of lateral spreading of the frontal co-ignimbrite cloud closely follows a linear relationship on log-log scales with slope of 1/8 (inset in Fig. 5a). It is thus similar to the spreading relationship of axisymmetric Boussinesq gravity currents in the viscous-buoyancy regime (Huppert and Simpson, 1980).

3.3. Thermal characteristics

An important difference between traditional aqueous gravity current experiments and real-world PDCs is the presence of hot volcanic particles that can heat and thermally expand the gas phase. In the hot gas-particle flows, most of the thermal energy is carried by the solid phase. Because thermal energy is mostly lost by particle deposition, temperature data can be used as a proxy for the current particle concentration.

The spatial resolution of our thermal data is slightly too low to clearly depict the internal density discontinuities (Fig. 6). During regime 1 (0.6 s in Fig. 6), and due to the vigorous entrainment of air during the free fall and impact stages, the gravity current is relatively cold, while the majority of the (hot) solids (and associated thermal energy) is still in free fall. Regime 2 (2.1 s in Fig. 6) is characterized by the intrusion of markedly hotter material from behind into the colder leading, highly entraining region of the current. The depth of the hot intrusion of higher particle concentration is limited upwards to the body-wake boundary. This also shows that mixing with ambient air, in this phase, is limited to the gravity current wake. Advective heating upwards from the body into the wake region only commences at the middle of regime 2 (3.6 s in Fig. 6). The transition between regimes 2 and 3 (6 s in Fig. 6) roughly coincides with the time when the gravity current head attains its temperature maximum during runout due to sufficient replacement of entrained ambient air with hot material from the concentrated intrusion from behind. From regime 3 onwards, the hitherto downstream propagating thermal intrusion reverses and migrates backwards (9.5 and 23 s in Fig. 6). This is due to the sufficient dilution of the gravity current and loss of (hot) particles due to sedimentation. In both the body and head regions, the temperature decreases with time, while the wake and upper head regions are seen to buoyantly rise upwards indicating vigorous mixing of the body and wake regions in regimes 3 and 4.

As investigated by Andrews (2014), heated and turbulent gas-particle gravity currents entrain ambient air primarily through their lateral flow margins, which is more efficient than vertical entrainment, i.e., through the flow front or upper flow margins. Mechanisms of lateral flow entrainment and its efficiency need targeted laboratory studies on the generated experimental hot multiphase density current.

4. Discussion

4.1. Similarities and differences in dynamic behaviour of dilute PDCs and aqueous gravity current analogues

The kinematic characteristics of compositional and particle-laden aqueous gravity currents with low- (Boussinesq) and high-density ratios (non-Boussinesq) are well studied through systematic series of lock-exchange laboratory experiments. Low-density ratio currents, following a brief phase of acceleration from rest, undergo:

1. a so-called slumping phase of constant velocity
2. an inertia-buoyancy phase where inertial and buoyancy forces are balanced, and
3. a viscous-buoyancy phase where viscous and buoyancy forces are balanced.

The transition between phases (1) and (2) occurs when a bore wave, initiated during lock withdrawal propagates backwards, is reflected by the channel end wall, and catches up with the advancing head (Rottman and Simpson, 1983). In PDCs and snow avalanches there is no lock-gate and channel back wall, and dynamic phase transitions must be associated with other physical processes. Importantly, in aqueous gravity currents, the characteristic non-dimensional front velocity, that is the densimetric Froude number (defined in Eq. (1)), is found to be approximately constant and close to a critical condition of 1.19 (Huppert and Simpson, 1980) or $\sqrt{2}$ (von Karman, 1940; Benjamin, 1968) throughout the entire flow propagation.

Systematic lock-exchange experiments on high-density particle-laden (turbidity) currents have demonstrated more complex phase transitions at conditions of increasing density differences between the current and aqueous ambient fluid (Hallworth and Huppert, 1998; Amy et al., 2005). For instance, at high flow densities, viscous water-particle slurry underflows develop at conditions of low Reynolds numbers and such turbidity currents may omit an inertia-buoyancy phase and transition directly from the slumping phase (1) to the viscous phase (3). Despite these complexities, kinematic models for high-density gravity currents typically assume a constant Froude condition for the gravity current (e.g. Gladstone and Woods, 2000; Nield and Woods, 2004; Dufek, 2016; Shimizu et al., 2021).

Our experimental high-Reynolds number and hot dilute PDCs, as well as real-world currents, differ in the following aspects:

1. They are characterized by a strong, power-law decrease in flow density during runout, which passes from an initial non-Boussinesq phase (density stage 1) into Boussinesq stages of a negatively buoyant phase (density stage 2), a partially positively buoyant phase (density stage 3) through to a fully positively buoyant plume phase (density stage 4).
2. Rather than a brief acceleration and slumping phase, the dilute PDCs initially undergo a strong deceleration during which the current is supercritical and the inertial force is two- to four-times larger than the buoyancy force. During the supercritical, dynamic regime 1 (corresponding to density stage 1), any density perturbation in the tail cannot reach the front of the highly supercritical current, which is thus ‘unaware’ yet of its finite length. In that regard, this situation is indeed comparable to the slumping phase of aqueous gravity currents when the reflected bore wave has not travelled back to the front yet (see for instance Ungarish (2009)). The transition to dynamic regime 2 (of converging inertial-buoyancy forces) is associated with the arrival of the first density discontinuity into the head. This density discontinuity moves at the theoretical velocity of internal gravity waves (Brosch et al., 2021) and propagates information about the finite extent of the current and is one of the characteristics that demonstrate that these flows are not strictly front-controlled. Instead, their dynamics are sensitive to the propagation of flow momentum through the gravity current body downstream. The intrusion of density discontinuities is characteristic for the entire dynamic regime 2.
3. Dynamic regime 2 transitions into dynamic regime 3 when internal gravity waves cease to advance into the front. The consequent feeding of the current head with heat and momentum (that is the density discontinuities and velocity associated with the brief but strong accelerations) is important for hazard considerations. High velocities minimizing chances of escape, high dynamic impact pressures, heat causing large burn risk, and high density of the ash-rich solid phase of PDCs associated with extreme suffocation risk, are high and largely unsteady during dynamic regime 2. In our 124 kg experiment, this regime characterizes about half of the flow runout length. In additional experiments with larger initial mass (200 and 300 kg), longer discharges (c. 8.2 and 15.1 s, respectively) and also higher initial flow density (c. 6.3–6.7 kg m^{-3}, respectively), the duration and spatial proportion of the current propagating under dynamic regime 2 increases significantly. This is associated with a larger number of internal density discontinuities being generated,

which continue propagating into the head over longer distances than in the 124 kg experiment. A detailed presentation of these results is planned for a future publication.

4. During dynamic regimes 3 and 4 (corresponding to density stages 3 and 4), density ratios ρ_C/ρ_A are close to and eventually fall below unity. Hence, buoyancy forces become increasingly insignificant to drive the gravity current. In the reference frame moving with the front, ambient counterflow must move up and over the front, similarly to air moving up and over a moving car. The pressure drag force associated with this process acts to slow down the front. In dynamic regime 3, the pressure drag force becomes the main force that retards the current, which is approaching a balance of inertial, and pressure drag forces. This is different than aqueous gravity currents that are characterized by a final stage of balanced buoyancy and viscous forces. Furthermore, in this final stage of unconfined propagation, entrainment from the lateral margins of the propagating flow aids in further decreasing the density and slowing down the current. This process has been previously described by Andrews (2014) who reports that for heated currents lateral entrainment is stronger than vertical entrainment from the flow front and top flow margins.
5. Finally, the distance, at which the flow becomes fully positively buoyant, and a hot phoenix (or co-ignimbrite) cloud develops as series of vertically rising plumes above the gravity current during dynamic regime 4, is highly sensitive to the initial density ratio (influenced for instance by the temperature of the ambient air), the initial mass flux and discharge duration. Similar results were recently obtained by Calabrò et al. (2022) in systematic numerical simulations of PDCs.
6. With regards to modelling and estimation of PDC runout limits, this indicates the importance of accurately capturing deposition and thereby improving the manner in which density and temperature decay in PDC models used to inform hazard mitigation.

4.2. Kinematic gravity current models

As real-world PDCs are inherently difficult and dangerous to probe directly, the application of experimental results from compositional and particle-laden aqueous gravity currents has been a powerful tool for the development of analytical and simplified numerical PDC models (e.g. Nield and Woods, 2004). These models have been important to better understand controlling mechanisms underlying PDC propagation (Bursik and Woods, 1996; Dade and Huppert, 1996; Choux et al., 2004; Dufek, 2016; Shimizu et al., 2021). Further, due to their computational simplicity, these usually one- or two-dimensional models lend themselves to estimate hazard probability through the computation of a wide range of plausible PDC starting and boundary conditions.

In the following we test some of these one-dimensional models for confined flows against our experimental results. The models considered are (i) the front velocity model for Boussinesq currents u_B (Yih, 1965):

$$u_B = \left(\frac{gh_C(\rho_C - \rho_A)}{\rho_C + \rho_A}\right)^{\frac{1}{2}} \tag{7}$$

(ii) the velocity box-model for non-Boussinesq currents for dense intrusions $u_{NB,D}$ (Nield and Woods, 2004):

$$u_{NB,D} = 1.2\sqrt{2}\,\rho^* + 2.2\left(\frac{\rho^*}{2-\rho^*}\right)^{6.6}\sqrt{gh_C} \tag{8}$$

and (iii) the characteristic wave velocity u_W in shallow water models, which is the maximum velocity that cannot be exceeded by flow-internal disturbances (Jacobsen and Fanneløp, 1984):

$$u_W = \left(\frac{gh_C(\rho_C - \rho_A)}{\rho_C}\right)^{\frac{1}{2}} \tag{9}$$

The results of the comparison of experimentally measured and modelled front velocities are shown in Fig. 7. All of the considered box- and shallow-water models strongly underestimate the actual front velocity by at least 25 and up to 95% for at least 90% of the runout length. We suggest that this deviation is considered with care for the applications of these and related one- and two-dimensional models that aim at estimating volcanic risk for public safety. The two main reasons for these significant deviations are as follows. First, unlike aqueous particle-laden gravity currents, dilute PDCs are not characterized by a critical constant Froude number. Second, the momentum carried by particles, particle sedimentation, entrainment of ambient air and thermal expansion are significant in the spatiotemporal evolution of flow density. We suggest that future research attempts to derive fundamental relationships that describe the evolution of flow density and Froude number.

Recently, Shimizu et al. (2021) tested a two-layer shallow-water model against our experimental data as part of the current international PDC validation and benchmarking exercise. In this model, the researchers use a constant critical densimetric Froude number as a model closure condition. Furthermore, they empirically fit a constant sedimentation rate to describe mass exchange between an upper dilute and lower dense layer of the gravity current. This model cannot capture the detailed spatiotemporal variations in flow density and flow height. However, the modelled front velocities can be reproduced with marked accuracy. These results highlight the potential of further developments of two-layer or multiple-layered shallow-water models for PDCs and related gas-particle gravity currents such as powder snow avalanches and dust storms.

5. Conclusion

In this study, we investigated the runout behaviour of hot dilute pyroclastic density currents (PDCs) in large-scale experiments and

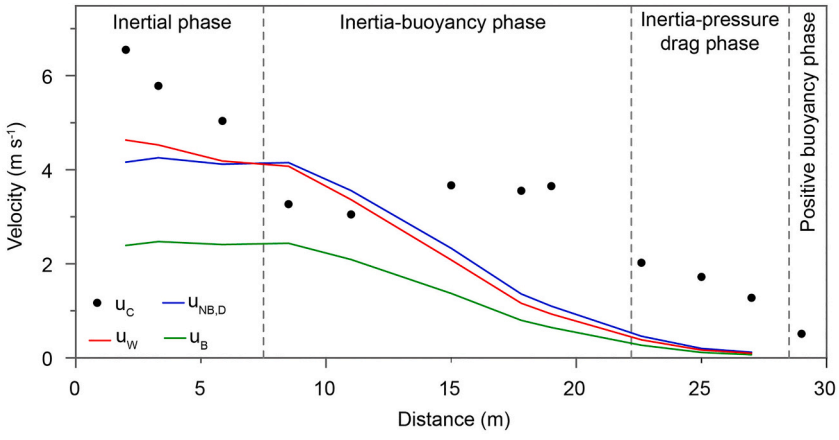

Fig. 7. A comparison of the evolution of front velocities with modelled velocities. The measured velocities u_C (filled circles) against distance are shown together with the modelled velocities using the Boussinesq gravity current model u_B (Eq. (7)) of Yih (1965); the non-Boussinesq gravity current model for dense intrusions $u_{NB,\,D}$ (Eq. (8)) of Nield and Woods (2004); and the shallow-water gravity current model u_W (Eq. (9)) initially proposed by Jacobsen and Fanneløp (1984) and applied to intrusions of dense gases into lighter ambient air by Gröbelbauer et al. (1993).

interrogated the similarities and differences to aqueous particle-laden gravity currents with low- and high-density differences to the ambient fluid. The main conclusions can be summarized as follows:

PDCs undergo four characteristic phases of dynamic behaviour of variable deceleration rates including: (i) an initial deceleration during dominance of inertial forces at high density difference between current and ambient fluid; (ii) a second phase where inertial and buoyancy forces almost approach a balance while the density difference decreases further; (iii) a third stage where the pressure drag force becomes the main retarding force while the current density approaches that of the ambient; and (iv) a fourth phase where the hot current becomes positively buoyant and the gravity current transitions into a plume.

The transition from the first to the second stage is governed by the arrival of a first internal pulse (density discontinuity travelling at the velocity of internal gravity waves) into the gravity current head and the current realizing its finite length. In the second stage, the arrival of internal gravity waves into the current head is associated with sudden accelerations and a replenishment of momentum and thermal energy with strong consequences for local increases in hazard magnitudes. The transition from the second to the third stage is associated with a critical distance beyond which internal gravity waves do not reach the advancing gravity current head anymore. The transition between the third and fourth stages at the moment of buoyancy reversal is highly sensitive to the discharge duration and associated number of generated large-scale coherent structures and internal pulses and the temperature contrast of the current with the ambient air.

During PDC runout, the Froude number is not constant. Assuming a constant Froude number leads to strong underprediction of flow velocity in analytical gravity current models for approximately half of the runout length. These findings are critical to the adaptation of hazard models for both dilute PDCs and other turbulent gas-particle gravity currents such as powder snow avalanches.

Supplementary data to this article can be found online at https://doi.org/10.1016/j.jvolgeores.2022.107697.

CRediT authorship contribution statement

E. Brosch: Conceptualization, Methodology, Investigation, Formal analysis, Writing – original draft, Writing – review & editing, Visualization. **G. Lube:** Conceptualization, Methodology, Resources, Writing – original draft, Writing – review & editing, Funding acquisition. **T. Esposti-Ongaro:** Writing – review & editing. **M. Cerminara:** Software, Writing – review & editing. **E.C.P. Breard:** Writing – review & editing. **E. Meiburg:** Writing – review & editing.

Declaration of Competing Interest

The authors declare that they have no known competing financial interests or personal relationships that could have appeared to influence the work reported in this paper.

Data availability

Data will be made available on request.

Acknowledgments

We thank A. Moebis, E. Nisbet and K. Kreutz for assistance with the experimental and laboratory aspects of this study. This study was supported by the Royal Society of New Zealand Marsden Fund (contract no. MAU1506 and MAU1902), the New Zealand Natural Hazards Research Platform (contract no. 2015-MAU-02-NHRP) and the Resilience to Nature's Challenges National Science Challenge Fund New Zealand (GNS-RNC047). This research was supported in part by the National Science Foundation under PHY-1748958. ECPB was supported by UKRI with the NERC-IRF (NE/V014242/1). For the purpose of open access, the author has applied a Creative Commons Attribution (CC BY) licence to any Author Accepted Manuscript version arising from this submission. We thank B. Andrews and O. Roche for thoughtful reviews that strengthened the manuscript. J. Gardner is thanked for editorial handling.

References

Amy, L.A., Hogg, A.J., Peakall, J., Talling, P.J., 2005. Abrupt transitions in gravity currents. J. Geophys. Res.-Earth Surf. 110 (F3). F03001.
Ancey, C., 2004. Powder snow avalanches: approximation as non-Boussinesq clouds with a Richardson number–dependent entrainment function. J. Geophys. Res. Earth Surf. 109 (F1).
Andrews, B.J., 2014. Dispersal and air entrainment in unconfined dilute pyroclastic density currents. Bull. Volcanol. 76 (9), 852.
Andrews, B.J., Manga, M., 2012. Experimental study of turbulence, sedimentation, and coignimbrite mass partitioning in dilute pyroclastic density currents. J. Volcanol. Geotherm. Res. 225, 30–44.
Azpiroz-Zabala, M., Cartigny, M.J.B., Talling, P.J., Parsons, D.R., Sumner, E.J., Clare, M. A., Simmons, S.M., Cooper, C., Pope, E.L., 2017. Newly recognized turbidity current structure can explain prolonged flushing of submarine canyons. Sci. Adv. 3 (10), e1700200.
Benjamin, T.B., 1968. Gravity currents and related phenomena. J. Fluid Mech. 31 (2), 209–248.
Birman, V.K., Martin, J.E., Meiburg, E., 2005. The non-Boussinesq lock-exchange problem. Part 2. High-Resolut. Simul. J. Fluid Mech. 537, 125–144.
Bonnecaze, R.T., Huppert, H.E., Lister, J.R., 1993. Particle-driven gravity currents. J. Fluid Mech. 250, 339–369.
Borden, Z., Meiburg, E., 2013. Circulation based models for Boussinesq gravity currents. Phys. Fluids 25 (10), 101301.
Breard, E.C.P., Lube, G., Jones, J.R., Dufek, J., Cronin, S.J., Valentine, G.A., Moebis, A., 2016. Coupling of turbulent and non-turbulent flow regimes within pyroclastic density currents. Nat. Geosci. 9 (10), 767–771.
Brosch, E., Lube, G., 2020. Spatiotemporal sediment transport and deposition processes in experimental dilute pyroclastic density currents. J. Volcanol. Geotherm. Res. 401, 106946.
Brosch, E., Lube, G., Cerminara, M., Esposti-Ongaro, T., Breard, E.C.P., Dufek, J., Sovilla, B., Fullard, L., 2021. Destructiveness of pyroclastic surges controlled by turbulent fluctuations. Nat. Commun. 12 (1), 7306.
Burgisser, A., Bergantz, G.W., 2002. Reconciling pyroclastic flow and surge: the multiphase physics of pyroclastic density currents. Earth Planet. Sci. Lett. 202 (2), 405–418.
Burgisser, A., Bergantz, G.W., Breidenthal, R.E., 2005. Addressing complexity in laboratory experiments: the scaling of dilute multiphase flows in magmatic systems. J. Volcanol. Geotherm. Res. 141 (3–4), 245–265.
Bursik, M.I., Woods, A.W., 1996. The dynamics and thermodynamics of large ash flows. Bull. Volcanol. 58 (2–3), 175–193.
Calabrò, L., Esposti Ongaro, T., Giordano, G., de Michieli Vitturi, M., 2022. Reconstructing pyroclastic currents' source and flow parameters from deposit characteristics and numerical modelling: the Pozzolane Rosse ignimbrite case study (Colli Albani, Italy). J. Geophys. Res. Solid Earth 127 (5) e2021JB023637.
Choux, C.M., Druitt, T.H., 2002. Analogue study of particle segregation in pyroclastic density currents, with implications for the emplacement mechanisms of large ignimbrites. Sedimentology 49 (5), 907–928.
Choux, C., Druitt, T., Thomas, N., 2004. Stratification and particle segregation in flowing polydisperse suspensions, with applications to the transport and sedimentation of pyroclastic density currents. J. Volcanol. Geotherm. Res. 138 (3–4), 223–241.
Dade, W.B., Huppert, H.E., 1996. Emplacement of the Taupo ignimbrite by a dilute turbulent flow. Nature 381 (6582), 509–512.
Dai, A., 2014. Non-Boussinesq gravity currents propagating on different bottom slopes. J. Fluid Mech. 741, 658–680.
Dellino, P., Zimanowski, B., Buttner, R., La Volpe, L., Mele, D., Sulpizio, R., 2007. Large-scale experiments on the mechanics of pyroclastic flows: design, engineering, and first results. J. Geophys. Res.-Solid Earth 112 (B4). B04202.
Dellino, P., Dioguardi, F., Doronzo, D.M., Mele, D., 2019. The entrainment rate of non-Boussinesq hazardous geophysical gas-particle flows: an experimental model with application to pyroclastic density currents. Geophys. Res. Lett. 46 (22), 12851–12861.
Druitt, T.H., 1998. Pyroclastic density currents. Geol. Soc. Lond., Spec. Publ. 145 (1), 145–182.
Dufek, J., 2016. The fluid mechanics of pyroclastic density currents. Annu. Rev. Fluid Mech. 48 (1), 459–485.
Gladstone, C., Woods, A.W., 2000. On the application of box models to particle-driven gravity currents. J. Fluid Mech. 416, 187–195.
Goudie, A.S., Middleton, N.J., 2001. Saharan dust storms: nature and consequences. Earth Sci. Rev. 56 (1), 179–204.
Gröbelbauer, H.P., Fanneløp, T.K., Britter, R.E., 1993. The propagation of intrusion fronts of high density ratios. J. Fluid Mech. 250, 669–687.
Hallworth, M.A., Huppert, H.E., 1998. Abrupt transitions in high-concentration, particle-driven gravity currents. Phys. Fluids 10 (5), 1083–1087.
Harris, T.C., Hogg, A.J., Huppert, H.E., 2001. A mathematical framework for the analysis of particle-driven gravity currents. Proc. R. Soc. Lond. A Math. Phys. Eng. Sci. 457 (2009), 1241–1272.
Hopfinger, E.J., 1983. Snow avalanche motion and related phenomena. Annu. Rev. Fluid Mech. 15 (1), 47–76.

Hughes Clarke, J.E., 2016. First wide-angle view of channelized turbidity currents links migrating cyclic steps to flow characteristics. Nat. Commun. 7 (1), 11896.
Huppert, H.E., 2006. Gravity currents: a personal perspective. J. Fluid Mech. 554, 299–322.
Huppert, H.E., Simpson, J.E., 1980. The slumping of gravity currents. J. Fluid Mech. 99 (Aug), 785–799.
Jacobsen, Ø., Fanneløp, T.K., 1984. Experimental and Theoretical Studies in Heavy Gas Dispersion. Part II. Theory. Atmospheric Dispersion of Heavy Gases and Small Particles. Springer Berlin Heidelberg, Berlin, Heidelberg, pp. 407–418.
Lowe, R.J., Rottman, J.W., Linden, P.F., 2005. The non-Boussinesq lock-exchange problem. Part 1. Theory and experiments. J. Fluid Mech. 537, 101–124.
Lube, G., Breard, E.C.P., Cronin, S.J., Jones, J., 2015. Synthesizing large-scale pyroclastic flows: experimental design, scaling, and first results from PELE. J. Geophys. Res.-Solid Earth 120 (3), 1487–1502.
Lube, G., Breard, E.C.P., Esposti-Ongaro, T., Dufek, J., Brand, B., 2020. Multiphase flow behaviour and hazard prediction of pyroclastic density currents. Nat. Rev. Earth Environ. 1, 348–365.
Martin, J.E., Meiburg, E., Birman, V.K., 2006. High Resolution Simulation of Particle-Driven Lock-Exchange Flow for Non-Boussinesq Conditions. Direct and Large-Eddy Simulation VI. Springer, Netherlands, Dordrecht, pp. 567–574.
Meiburg, E., Kneller, B., 2010. Turbidity currents and their deposits. Annu. Rev. Fluid Mech. 42 (1), 135–156.
Moore, J.G., Rice, C.J., 1984. Chronology and character of the May 18, 1980, explosive eruptions of Mount St Helens. In: Council, N.R. (Ed.), Explosive Volcanism: Inception, Evolution, and Hazards. The National Academies Press, Washington, pp. 133–142.
Nield, S.E., Woods, A.W., 2004. Effects of flow density on the dynamics of dilute pyroclastic density currents. J. Volcanol. Geotherm. Res. 132 (4), 269–281.
Pope, E.L., Cartigny, M.J.B., Clare, M.A., Talling, P.J., Lintern, D.G., Vellinga, A., Hage, S., Açikalin, S., Bailey, L., Chapplow, N., Chen, Y., Eggenhuisen, J.T., Hendry, A., Heerema, C.J., Heijnen, M.S., Hubbard, S.M., Hunt, J.E., McGhee, C., Parsons, D.R., Simmons, S.M., Stacey, C.D., Vendettuoli, D., 2022. First source-to-sink monitoring shows dense head controls sediment flux and runout in turbidity currents. Science. Advances 8 (20) eabj3220.
Rottman, J.W., Simpson, J.E., 1983. Gravity currents produced by instantaneous releases of a heavy fluid in a rectangular channel. J. Fluid Mech. 135 (Oct), 95–110.
Rotunno, R., Klemp, J.B., Bryan, G.H., Muraki, D.J., 2011. Models of non-Boussinesq lock-exchange flow. J. Fluid Mech. 675, 1–26.
Scharff, L., Hort, M., Varley, N.R., 2019. First in-situ observation of a moving natural pyroclastic density current using Doppler radar. Sci. Rep. 9 (1), 7386.
Scott, D.H., Tanaka, K.L., 1982. Ignimbrites of Amazonis Planitia region of mars. J. Geophys. Res. Solid Earth 87 (B2), 1179–1190.
Shimizu, H.A., Koyaguchi, T., Suzuki, Y.J., Brosch, E., Lube, G., Cerminara, M., 2021. Validation of a two-layer depth-averaged model by comparison with an experimental dilute stratified pyroclastic density current. Bull. Volcanol. 83 (11), 73.
Simpson, J.E., Britter, R.E., 1979. The dynamics of the head of a gravity current advancing over a horizontal surface. J. Fluid Mech. 94 (3), 477–495.
Sovilla, B., Schaer, M., Kern, M., Bartelt, P., 2008. Impact pressures and flow regimes in dense snow avalanches observed at the Vallée de la Sionne test site. J. Geophys. Res. Earth Surf. 113 (F1).
Sovilla, B., McElwaine, J.N., Köhler, A., 2018. The intermittency regions of powder snow avalanches. J. Geophys. Res. Earth Surf. 123, 2525–2545.
Sulpizio, R., Dellino, P., Doronzo, D.M., Sarocchi, D., 2014. Pyroclastic density currents: state of the art and perspectives. J. Volcanol. Geotherm. Res. 283, 36–65.
Sweeney, M.R., Valentine, G.A., 2017. Impact zone dynamics of dilute mono- and polydisperse jets and their implications for the initial conditions of pyroclastic density currents. Phys. Fluids 29 (9), 093304.
Ungarish, M., 2009. An Introduction to Gravity Currents and Intrusions. CRC Press.
Valentine, G.A., Sweeney, M.R., 2018. Compressible flow phenomena at inception of lateral density currents fed by collapsing gas-particle mixtures. J. Geophys. Res. Solid Earth 123 (2), 1286–1302.
von Karman, T., 1940. The engineer grapples with nonlinear problems. Bull. Am. Math. Soc. 46 (8), 615–683.
Vriend, N.M., McElwaine, J.N., Sovilla, B., Keylock, C.J., Ash, M., Brennan, P.V., 2013. High-resolution radar measurements of snow avalanches. Geophys. Res. Lett. 40 (4), 727–731.
Wohletz, K.H., 1998. Pyroclastic surges and compressible two-phase flow. Dev. Volcanol. 4.
Yih, C.S., 1965. Dynamics of Nonhomogeneous Fluids. MacMillan.